Ambient seismic noise eikonal tomography for near-surface imaging at Valhall

Sjoerd de Ridder and Joe Dellinger

ABSTRACT

We demonstrate that in three passive seismic datasets recorded by an ocean-bottom-cable array at the Valhall field in the Norwegian North Sea, virtual-source interferometry over the frequency range 0.35-1.75 Hz produces strong omnidirectional Scholte-wave sources. We then use these virtual-sources gathers to image the shallow structure in high resolution using eikonal traveltime tomography. Unlike conventional tomography, which determines velocities between source and receiver using an inversion scheme, eikonal tomography computes the local traveltime gradient at each receiver, and thus directly estimates the local velocity in the neighborhood of each receiver. The Scholte-wave images produced from imaging the passive noise reveal many of the same features visible in the active P-wave data. These results suggest that a permanent recording system using passive seismic noise might be useful for real-time surveillance of shallow shear-wave velocity anomalies.

INTRODUCTION

The permanent ocean-bottom array at the Valhall field in Norway provides an excellent source of passive seismic data to test what might be accomplished with seismic interferometry. The array, installed in 2003 (Kommedal et al., 2004), can record data for long periods in all weather conditions. The subsurface structure is well known, both from numerous wells and from seismic imaging. During periods without active seismic acquisition at Valhall, there is abundant passive energy in the data over a wide range of frequencies. Previous attempts to synthesize omnidirectional point sources at conventional seismic exploration frequencies (3-60 Hz) failed at Valhall (Artman, 2007; Landes et al., 2009), so passive data will not replace active data in the higher frequencies ranges there. However, at lower frequencies (0.18-1.75 Hz), omnidirectional virtual Scholte-wave sources have been successfully generated (Dellinger and Yu, 2009; Bussat and Kugler, 2009; Dellinger et al., 2010). We process three passive datasets from the Valhall permanent array in Norway, generate virtual Scholte-wave source gathers using seismic interferometry, and then use these sources to image the shallow structure using eikonal traveltime tomography (Lin et al., 2009). Finally, we compare our results to the P-wave velocity structure at Valhall as determined from active data (Sirgue et al., 2010).

THE AMBIENT SEISMIC NOISE FIELD AT VALHALL

We use three OBC recordings of ambient seismic noise recorded at Valhall: 29 hours in 2004, 6.5 hours in 2005 in conditions that transitioned from calm to stormy, and 2 hours in 2008 recorded under stormy conditions as the remnants of tropical storm Laura passed over. Unlike the previous passive datasets, the 2008 dataset was recorded without the customary low-cut recording filter. Figure 1 shows spectra of the vertical component of the particle velocity for all three datasets. The ambient seismic field is excited by various noise sources that dominate in different frequency regimes (Olofsson, 2010). In the Valhall recordings, we distinguish five frequency regimes based on their distinctive spectral amplitudes and excitation mechanisms (Dellinger and Yu, 2009). Band A (< 0.18 Hz) contains energy from ocean swells. This energy has tremendous amplitude in the pressure component (which explains why low-cut recording filters are customary) but is virtually absent in the vertical component of the particle velocity sensor. Bands B (0.18-0.35 Hz) and C (0.35-1.75 Hz) contain microseism energy generated by the interaction of weather-generated ocean waves and the sea floor (Longuet-Higgins, 1950; Rhie and Romanowicz, 2004, 2006). In ocean acoustics, this band is referred to as the double-frequency microseism peak. This energy has proven to be suitably random in propagation direction, as required for interferometry.

Bands D (1.75-18 Hz) and E (> 18 Hz) contain human-generated noise associated with field operations, boats and distant seismic shooting. Note that repetitive artificial sources can be identified by the spiky character of their spectra. Natural sources are more random and result in relatively smooth spectra. When weather is calm and the microseism peak is weak, human-generated noise sources overwhelm the microseism energy at the upper end of the microseism band. This pushes the upper limit of useful microseism energy down during calm weather conditions. Thus ambient seismic-noise data is best recorded during stormy conditions and/or during periods with few noise-making field operations.

Weather records (NMI, 2011) indicate that the 2005 recording began in calm weather that then transitioned to stormy, a change that is readily apparent in the change in the spectrum over time windows. Weather records for the 2004 dataset are not available, but the data show that the 2004 dataset started under weather conditions even calmer than the start of the 2005 dataset, and ended under weather conditions somewhat less stormy than at the end of the 2005 dataset. Comparing the spectrum of the (unfiltered) 2008 recording with the (filtered) 2004 and 2005 recordings shows that the low-cut filter suppresses much of the microseism band of interest. In this paper we wish to compare results for all three datasets, and so we will perform our analysis for energy in frequency band C, between 0.35-1.75 Hz. Band C is highlighted in Figure 1. Seismic interferometry for microseism energy also succeeds in band B for the 2008 recording (Dellinger and Yu, 2009; Dellinger et al., 2010).

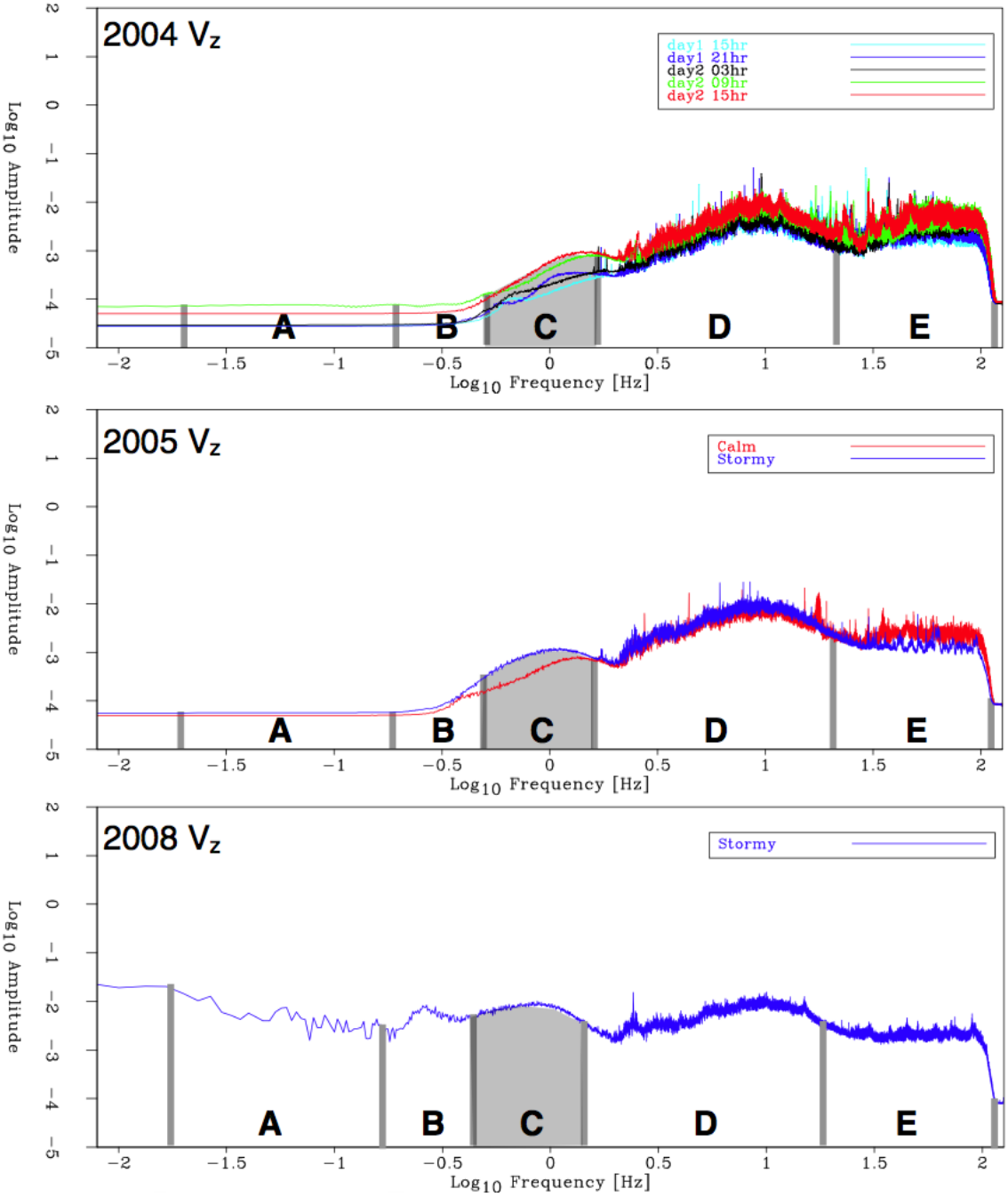

Figure 1: Frequency spectra of the vertical component of the particle velocity for the 2004 (top panel), 2005 (middle panel) and 2008 (bottom panel) datasets. We divide the data into five frequency bands labeled A to E. Band A ($<$ 0.18 Hz) is the frequency regime for ocean swells, bands B (0.18-0.35 Hz) and C (0.35-1.75 Hz) contain microseism energy, and in bands D (1.75- 18 Hz) and E ($>$ 18 Hz) human-generated noise dominates. The 2005 data have been subdivided into calm and stormy spectra. Five spectra for the 2004 dataset are shown, computed over consecutive 6-hour intervals. [**NR**]

EIKONAL TOMOGRAPHY

Tomography produces an estimated velocity field from a large number of measurements of travel time (or phase). Traditionally, a forward-modeling operator is constructed by solving the eikonal equation in a background velocity model for each observable data point. These data points then act as a global constraint on the inversion. The resulting linear system is typically solved by matrix inversion techniques, regularized by spatial smoothing and Tichonov regularization. In contrast, eikonal tomography (Lin et al., 2009) is a procedure that uses the spatial gradient of a traveltime map as a local constraint on the wave-speed map. This relation is described by the scalar eikonal equation (Aki and Richards, 2002):

$$|\nabla t_i(x)| = c_i^{-1}(x). \tag{1}$$

Evaluating this equation for one virtual-source gather leads to an estimate of the local wave velocity.

We perform ambient-seismic-noise eikonal tomography as follows: First, the data are bandpassed (for band C) and virtual-seismic source gathers are constructed by correlation. Figure 2a shows 30 seconds of bandpassed seismic noise recorded in the 2008 dataset by one line of the Valhall array. Figure 2b shows a virtual-source gather created by correlating 2 hours of noise along that line with the data for the station at the offset marked 0, located towards the right end of the line. For ideal ambient seismic noise, positive and negative time lags of the correlation should contain a symmetrized impulse response (Wapenaar and Fokkema, 2006). We stacked positive and negative time lags to enhance the quality of the created virtual-source gathers.

Next, traveltimes are estimated by picking the maximum value of the envelope function of the virtual-seismic-source data within a defined moveout window. Figure 2c shows picks for the virtual-source gather in figure 2b. We also calculate a signal-to-noise ratio (SNR) quality factor, defined as the amplitude of the envelope peak within the moveout window divided by the average amplitude outside the window. We keep only the traveltime picks exceeding a specified SNR and regularize them using biharmonic spline interpolation (Sandwell, 1987) (see Appendix). The traveltime map should only be interpreted for portions surrounded by picks that we kept. Next, we use equation 1 to estimate the local velocity at each point for waves from each virtual-source gather. The final step is to produce tomographic maps by statistically characterizing the estimates at each position in the model.

$$s_0(x) = \frac{1}{N}\sum_{i=1}^{N} s_i(x) \tag{2}$$

and

$$\sigma_s^2(x) = \frac{1}{N(N-1)}\sum_{i}^{N} \left(s_i(x) - s_0(x)\right)^2. \tag{3}$$

Figure 3 shows how this works. Figure 3a shows an amplitude snapshot for a virtual-source gather gather in the southern portion of the Valhall data for the 2008 dataset. Notice that the impulse response is nearly perfectly omnidirectional. Figure 3b shows regularized travel times across the array for this virtual-source. Note that more distant picks did not have a sufficient SNR and were discarded. Figure 3c shows a map of velocity estimates calculated using those regularized picked travel times. This process is repeated for each virtual-source gather, potentially producing a large number of velocity estimates.

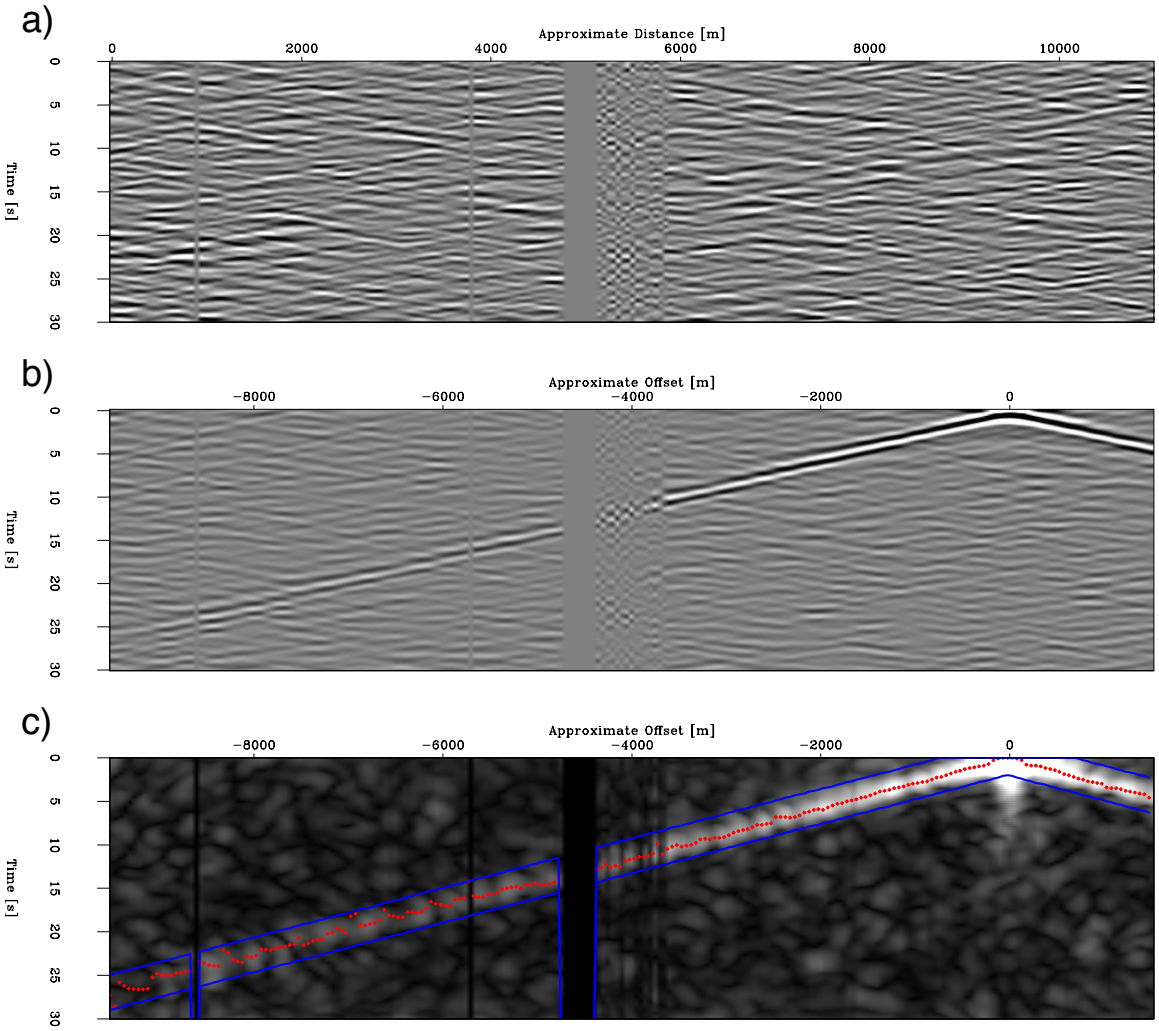

Figure 2: Three panels demonstrating the first half of the processing flow of ambient seismic noise eikonal tomography for a receiver line in the 2008 dataset: (a) 30 seconds of ambient seismic noise after bandpassing between 0.35 Hz and 1.75 Hz; (b) data from a virtual-source created at a station near the right end of the line; (c) travel-time picks superimposed on top of the envelope function of the virtual-seismic-source data in the middle panel. [**CR**]

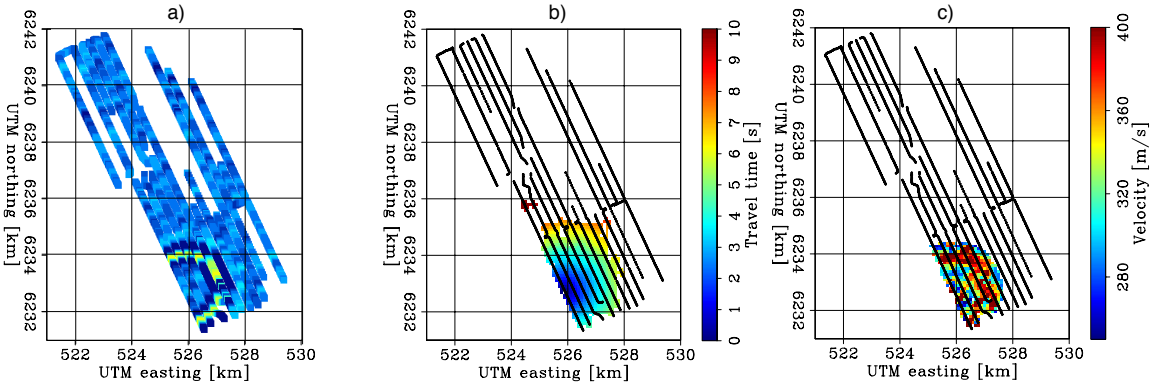

Figure 3: Three panels showing the continuation of the processing flow begun in Figure 2, traveltime map construction and velocity estimation for one virtual-source: (a) A snapshot showing Scholte-waves propagating away from a virtual-source in the southern portion of the Valhall array. The virtual-source was created using data from the 2008 dataset, bandpassed between 0.35 Hz and 1.75 Hz. (b) Regularized travel time surfaces picked from this virtual-source gather. (c) The resulting velocity estimates. [**NR**]

EXPLICIT INVERSION BY STATISTICS

Whereas for conventional seismic imaging, the inversion contains a wavefield extrapolation step (Claerbout, 1985), eikonal tomography finds an estimate of the model directly after merely regularizing the data. This possible because measurements are available throughout the domain of the model space. Different illuminations of the model by diferent sources are still added together through a weighted sum to find a composite model. Evaluating equation 1 for N virtual-source gathers, one at each receiver station, and applying the acceptence criteria mentioned above leads to a set of estimates of the local wave velocity at each receiver location $\mathbf{x}$.

A logarthmic histogram of the SNR of all picks in the Valhall array (Figure 4(a)) shows the large majority of picks have very low SNR. Generally the SNR ratio decreases quite rapidly with increasing source-receiver distance due to geometrical spreading (Figure 4(b)). The deficiency between SNR's of 30 to 40 and the jump in the SNR scatter plots at a radius of 750 m are related to the dispersion of the Scholte wave in the correlation gathers. They coincide with phase cycles, which are strongly reflected in the amplitude of the envelope function.

A complication with Gaussian statistics on measurements of velocity or slowness is that they are both always positive. Tarantola (2006) suggests these so called *Jeffreys quantities* are more safely analyzed in their logarithmic magnitudes. Here we briely disuss the model estimate distributions. The expected value and variance of the estimate sets are calculated on the estimates in three magnitudes: linear slowness, linear velocity and logarithm of velocity. For linear slowness magnitudes we have

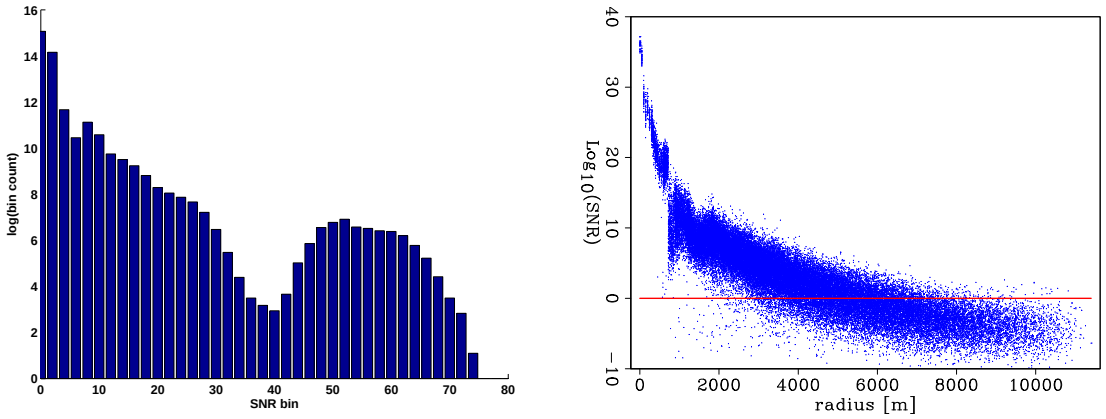

(a) (b)

Figure 4: a) Histogram of SNR. b) Scatter plot of 1% of all SNR's versus radius, line is the lower acceptence level. [**NR**] [**CR**]

(again)

$$s_0(x) = \frac{1}{N}\sum_{i=1}^{N} s_i(x) \tag{4}$$

and

$$\sigma_s^2(x) = \frac{1}{N(N-1)}\sum_{i}^{N} \left(s_i(x) - s_0(x)\right)^2 . \tag{5}$$

For linear velocity magnitudes we calculate

$$c_0(x) = \frac{1}{N}\sum_{i=1}^{N} c_i(x) \tag{6}$$

and

$$\sigma_c^2(x) = \frac{1}{N(N-1)}\sum_{i}^{N} \left(c_i(x) - c_0(x)\right)^2 . \tag{7}$$

When characterizing logarithmic slowness or velocity magnitudes an expected value and variance can be obtained from either slowness or velocity as

$$\ell_0(x) = -\frac{1}{N}\sum_{i=1}^{N} \log_{10}\left(s_i\right) = \frac{1}{N}\sum_{i=1}^{N} \log_{10}\left(c_i\right) \tag{8}$$

and

$$(\ell_\sigma)^2(x) = \frac{1}{N(N-1)}\sum_{i}^{N} \left(\log_{10}\left(s_i\right) + \ell_0\right)^2 = \frac{1}{N(N-1)}\sum_{i}^{N} \left(\log_{10}\left(c_i\right) - \ell_0\right)^2 . \tag{9}$$

The results of either approach are most intuitively compared in units of velocity (m/s). So the expected values are compared through:

$$c_0 \text{ with } s_0^{-1} \text{ and } 10^{\ell_0}. \tag{10}$$

The variances are compared through:

$$\sigma_c \text{ with } \frac{1}{s_0^2}\sigma_s \text{ and } \frac{1}{2}\ 10^{\ell_0}\left[10^{\ell}_{\sigma} - 10^{-\ell_\sigma}\right]. \tag{11}$$

The last term is the average between two velocity values corresponding to the expected value plus and minus the square-root of variance in logarithmic space.

Normal distributions are fitted to the estimates in Figures 5 and 6 on the respective magnitudes. For the estimates near a high-velocity anomaly we find $c_0 = 348$ m/s and $\sigma_c = 38.8$ m/s, $s_0 = 0.00290 \Rightarrow 345$ m/s and $s_\sigma = 0.000328 \Rightarrow 38.7$ m/s, and $\ell_0 = 2.54 \Rightarrow 346$ m/s and $\ell_\sigma = 0.0487 \Rightarrow 38.9$ m/s. For the estimates near a low-velocity anomaly we find $c_0 = 299$ m/s and $\sigma_c = 36.36$ m/s, $s_0 = 0.00339 \Rightarrow 295$ m/s and $s_\sigma = 0.000410 \Rightarrow 35.6$ m/s, and $\ell_0 = 2.47 \Rightarrow 297$ m/s and $\ell_\sigma = 0.0527 \Rightarrow 36.1$ m/s. For both estimate sets we find the expected value on the logarithmic velocity magnitude to be within the values of the expected value on the linear slowness and linear velocity magnitudes. However the deviations on these expected values are about 10 times smaller then the standard deviations on the estimates, regardless of which magnitudes are analyzed.

In Figures 5(d) and 6(d) Q-Q plots indicate how well the estimates fit normal distributions (plus symbols for slowness magnitudes, circles for velocity magnitudes and quandrangles for logarithmic velocity magnitudes). Q-Q plots for the different magnitudes carry a different unit on their vertical axis. The diagonal corresponds to a perfect fit. The intermediate quantiles follow Gaussian statistics quite well. In the lower and higher quantiles the data differs from a normal distribution. In the high-velocity anomaly (Figure 5(d)) the slowness magnitudes fit a normal distribution better in the lower quantiles and the velocity magnitudes better in the higher quantiles (not surprising because velocity is inverse slowness). In the low-velocity anomaly (Figure 6(d)) the logarithmic velocity magnitudes fit a normal distribution best in the lower quantiles while the velocity magnitudes better in the higher quantiles.

These observations might not hold in general for low- and high-velocity anomalies. Fortunately, the choice of which magnitude to use to analyze the gradient estimates does not significantly change the resulting tomography maps. Gaussian statistics do not adequately fit the tails of the estimate sets. For simplicity we chose to base the tomographic images on the expected value of a linear slowness basis. For this data, the variance is a very limited measure and does not infer an estimate certainty in a Gaussian statistics sense. Thus two additional quality measures of the expected value are the density of accepted picks and the velocity-estimate density. The first is a (regularized) map of the number of accepted travel time picks per station. The second is simply a map of N, the number of raw travel time measurements available at that location.

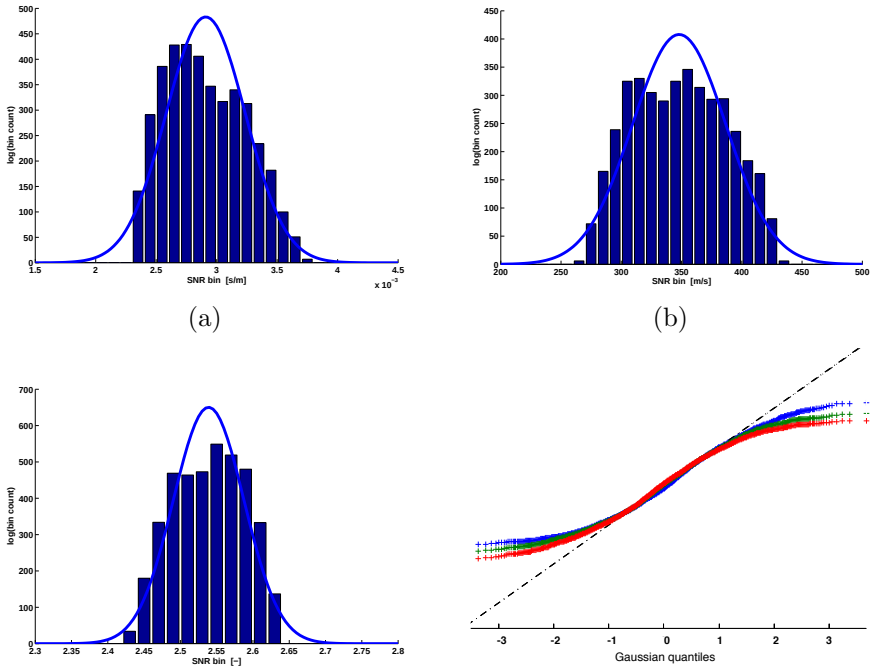

Figure 5: Histograms and their normal distribution fits of the gradient estimates in a high velocity region: a) linear slowness magnitude, b) linear velocity magnitude, c) logarithmic velocity magnitude, d) normal Q-Q plots of the gradient magnitudes (plus symbols: linear slowness, circles: linear velocity, quandrangles: logarithmic velocity). [**CR**] [**CR**] [**CR**] [**NR**]

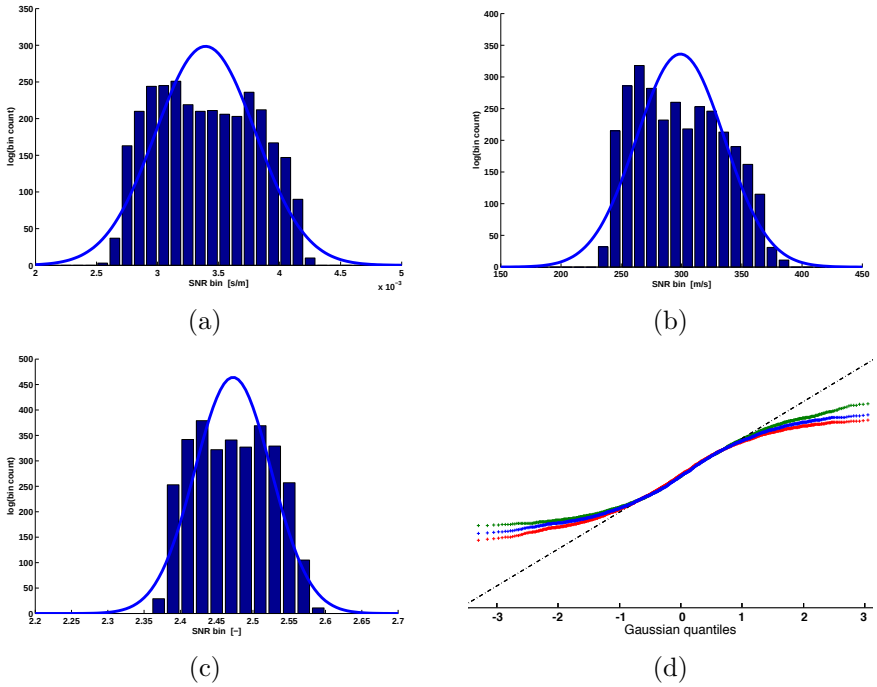

Figure 6: Histograms and their normal distribution fits of the gradient estimates in a low-velocity region: a) linear slowness magnitude, b) linear velocity magnitude, c) logarithmic velocity magnitude, d) normal Q-Q plots of the gradient magnitudes (plus symbols: linear slowness, circles: linear velocity, quandrangles: logarithmic velocity). [**CR**] [**CR**] [**CR**] [**NR**]

SCHOLTE-WAVE VELOCITY MAPS

Correlations were performed for time blocks of at most 3 hours. Signal to noise ratios were calculated using a moveout window 4 seconds wide centered on a moveout-velocity trajectory of 350 m/s. For the inversion we only used picks with SNRs of over 2 that were located within a radius of 1750 m of the virtual-source gather. We found the eikonal tomography results to be more improved by excluding picks at larger offsets than by elevating the SNR threshold. Further offsets might get sensitive to deeper structures or contain other wavemodes. Thus the gradients would fundamentally start to conflict. Figures 7-9 contain images of Scholte-wave velocities and quality factors obtained by performing eikonal tomography on the 2004, 2005 and 2008 datasets, respectively. The top left panels show the expected-value velocity maps, and the top right panels show the associated standard deviations. The lower left and right panels show maps of the regularized pick density and the number of estimates (N), respectively. For comparison, Figure 10 shows maps of estimated P-wave (not Scholte-wave) velocities between 60 and 105 m (in Figure 10a) and between 150 and 195 m (in Figure 10b) beneath the ocean floor. This result was obtained by Sirgue et al. (2010) using full-waveform inversion (FWI) between 3.5 Hz and 7 Hz on a conventional active seismic dataset.

Several high- and low-velocity anomalies can be distinguished in the Scholte-wave maps from the 2004 and 2005 data. These appear to correspond to structures also observable in the P-wave velocity map. The high-velocity anomalies are interpreted to be channel features (indicated by arrows). Dotted circles indicate two distinct low-velocity zones. The FWI inversion was performed for frequencies higher than those in this eikonal tomography study, so it is not surprising that the tomographic images of Scholte-wave velocities obtained from the eikonal tomography lack the short-wavelength resolution of the P-wave velocity map obtained from FWI.

The traveltime map estimated from the 2008 dataset contains generally higher velocitiesthan the traveltime maps from the 2004 and 2005 datasets. This might be because the (unfiltered) 2008 dataset contains stronger low frequencies, and thus is more sensitive to higher velocities deeper in the Earth. However, parts of the 2008 map (especially in the South) bear little resemblance to the 2004 or 2005 maps, or to the structures in the P-wave velocity map. Only 2 hours of data were available from 2008, and as a result the SNRs of the virtual-source gathers generally were lower. The 2008 Scholte-wave velocity map was thus constructed using far fewer accepted picks than the maps of 2004 and 2005, so the map from the 2008 dataset may simply be unreliable. Availability of longer data sets recorded without a low-cut filter would enable further investigation of the application of the lower frequencies in the microseism energy to subsurface imaging.

Note the isolated low near the center of the array in the pick-density map for the 2004 eikonal inversion. This receiver station was probably malfunctioning (or possibly was simply mislocated) and slipped through initial quality control. It did not damage the results, however, because it was discarded by the automated picking

algorithm. The P-wave velocity map in Figure 10b prominently displays a large meandering channel that passes under the extreme southeastern part of the array. This channel is deeper than the narrower channels marked by the meandering dotted arrows in Figure 10b. There is no corresponding anomaly in the eikonal result for the 2004 data. There are anomalies in the 2005 and 2008 data at approximately the right location, but they are certainly not conclusive matches. It is possible that the lower-frequency, deeper-sensing 2008 dataset might be detecting that channel. Unfortunately the edges of the array have relatively few travel times to work with, so this remains inconclusive. Note that FWI was able to use active sources, which covered a wider area, to image well outside the receiver array even at these shallow depths. Interferometry uses the receivers as sources and so has a more restricted image space.

CONCLUSIONS

The ambient seismic field at Valhall contains omnidirectional noise suitable for seismic noise tomography at low frequencies between 0.35 Hz and 1.75 Hz. Scholte-waves traveling along the ocean floor can provide a tomographic image of features in the near surface (between 0 and 105 meters beneath the ocean floor). We have demonstrated that eikonal tomography is an effective tool for studying surface waves at Valhall, even though the gradient estimate sets do not closely resemble Gaussian distributions. This research shows that there is potential for developing a low-cost near-surface monitoring system using passive noise recorded by permanent ocean-bottom arrays.

ACKNOWLEDGEMENTS

This research was initiated as part of a summer internship at BP America by S. de Ridder under the supervision of Joe Dellinger. The authors would like to thank Ray Abma, Olav Barkved, John Etgen, Phuong Vu, and Jianhua Yu for helpful discussions and suggestions. We also thank BP and the partners of the Valhall Field (BP Norge and Hess Norge) for permission to publish this paper. S. de Ridder would like to acknowledge Biondo Biondi, Jon Claerbout, Bob Clapp and Andre Journel for fruitful discussions and the sponsors of the Stanford Exploration Project for their financial support.

REFERENCES

Aki, K. and P. G. Richards, 2002, Quantitative Seismology - second edition: University Science Books.

Artman, B., 2007, Passive seismic imaging: PhD thesis, Stanford University.

Bussat, S. and S. Kugler, 2009, Recording noise - estimating shear-wave velocities: Feasibility of offshore ambient-noise surface-wave tomography (answt) on a reservoir scale: SEG Technical Program Expanded Abstracts, **28**, 1627–1631.

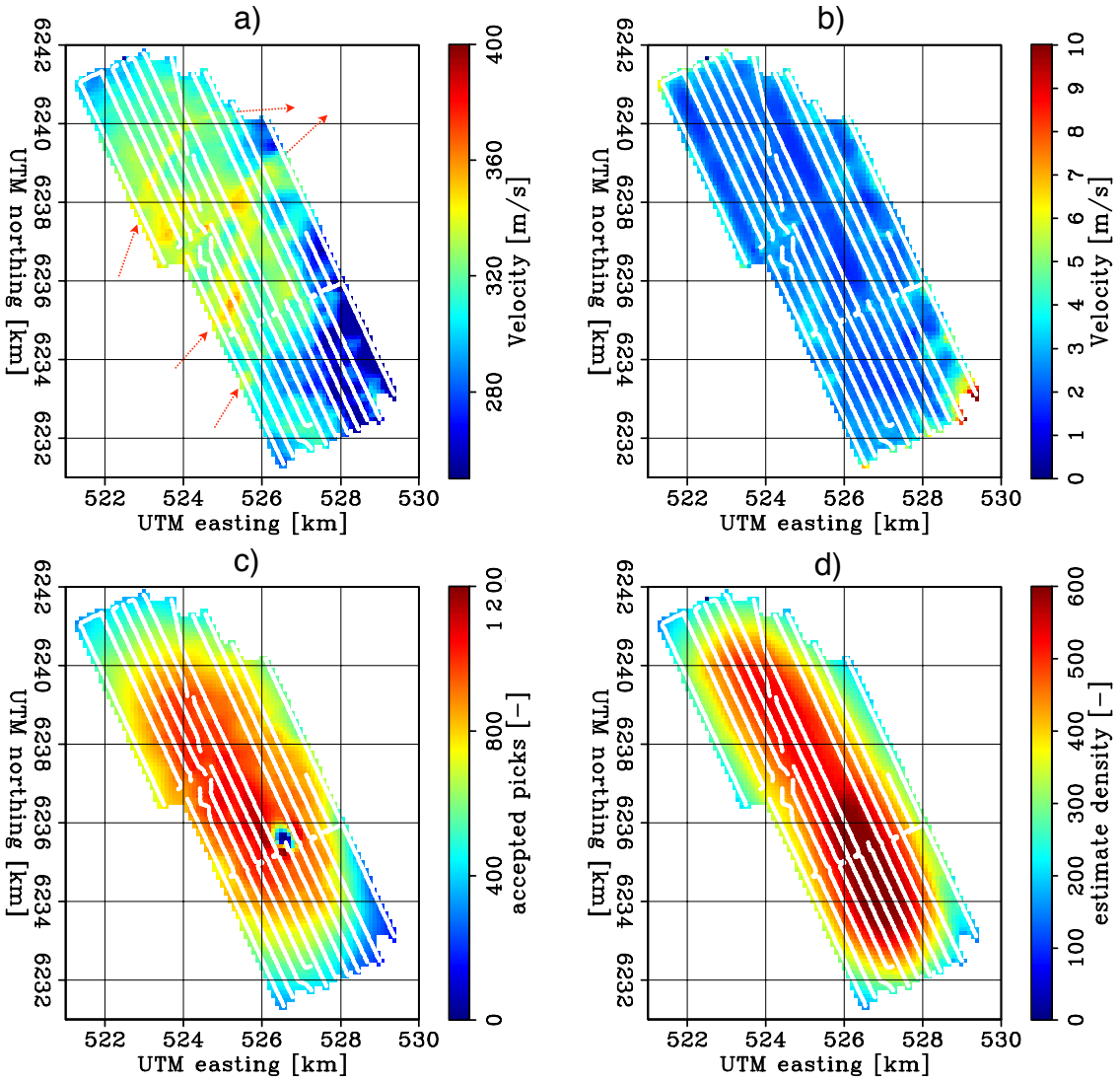

Figure 7: Images of Scholte-wave velocities and uncertainties obtained from eikonal tomography on the 2004 dataset; the expected value (a), the standard deviation of velocity (b), pick density at each station (c), and the number of velocity estimates at each grid point (d). Dotted arrows in (a) indicate channel features. [**CR**]

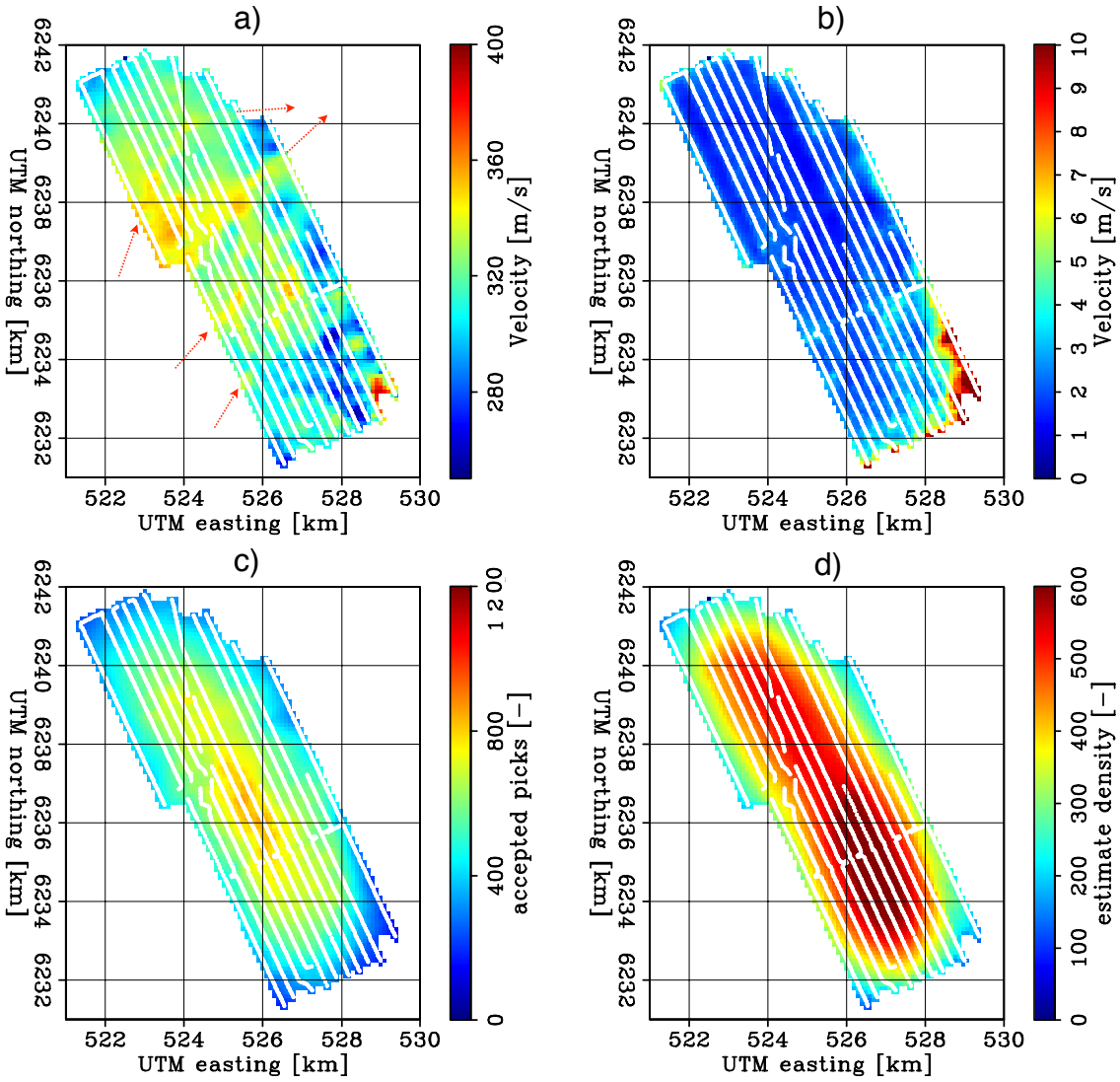

Figure 8: Images of Scholte-wave velocities and uncertainties obtained from eikonal tomography on the 2005 dataset; the expected value (a), the standard deviation of velocity (b), pick density at each station (c), and the number of velocity estimates at each grid point (d). Dotted arrows in (a) indicate channel features. [**CR**]

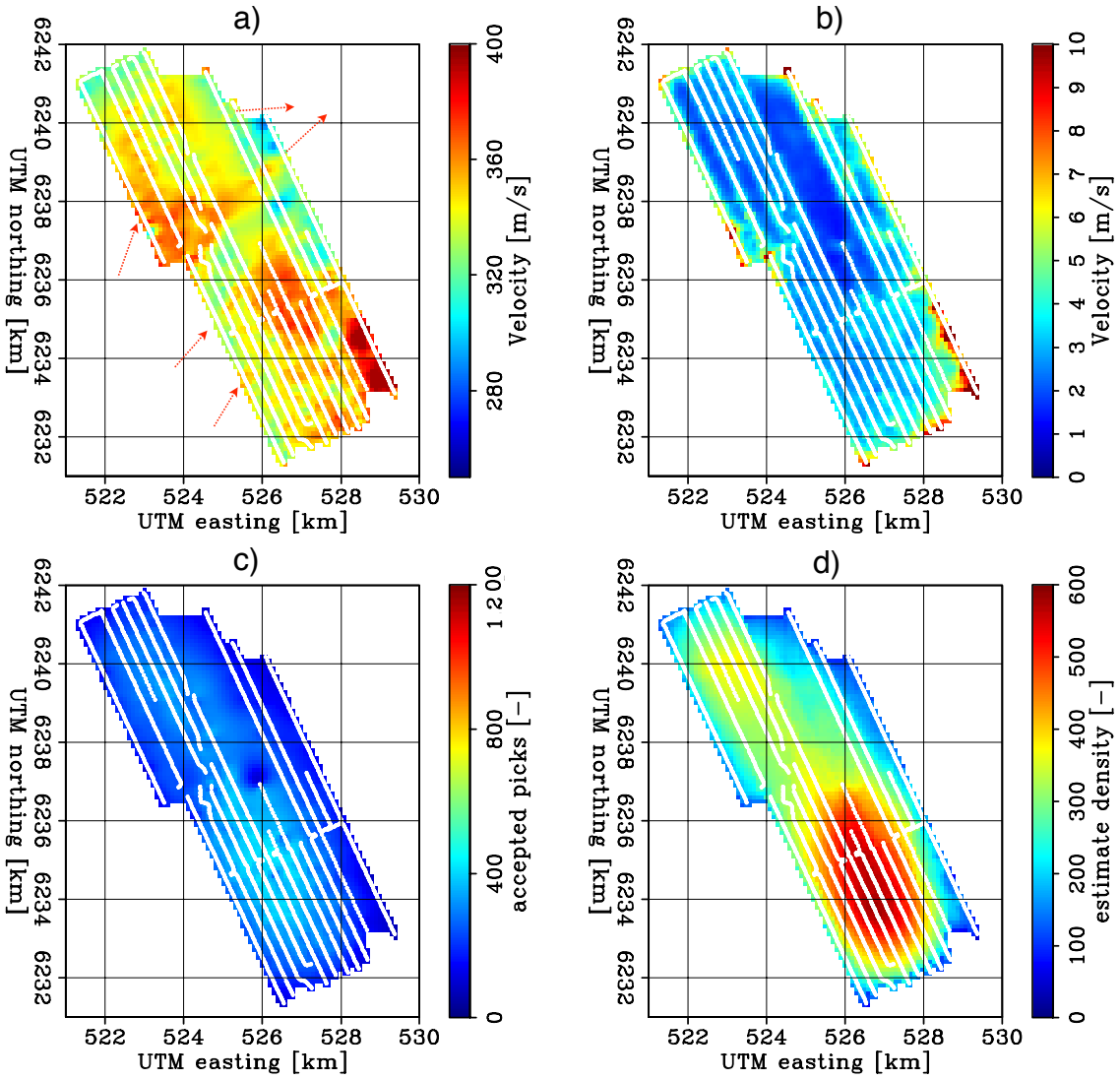

Figure 9: Images of Scholte-wave velocities and uncertainties obtained from eikonal tomography on the 2008 dataset; the expected value (a), the standard deviation of velocity (b), pick density at each station (c), and the number of velocity estimates at each grid point (d). Dotted arrows in (a) indicate channel features. This dataset produces a distinctly different result from the other two, possibly because it was recorded without a low-cut recording filter. [**CR**]

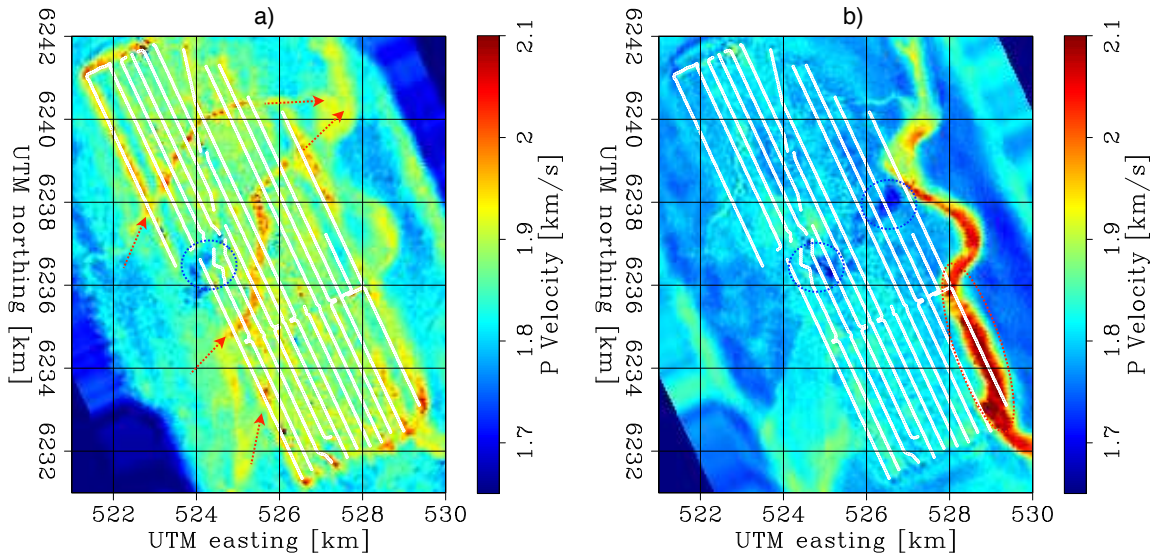

Figure 10: Images of average P-wave velocities obtained using waveform inversion (Sirgue et al., 2010) of active P-wave data; (a) between 60 and 105 m beneath the ocean floor, and (b) between 150 and 195 m beneath the ocean floor. Dotted arrows indicate channel features; dotted circles indicate two distinct low-velocity zones. [**NR**]

Claerbout, J. F., 1985, Imaging the earth's interior: Blackwell Scientific Publications.

Dellinger, J., J. Yu, and S. de Ridder, 2010, Virtual-source interferometry of 4C OBC data at Valhall without a low-cut recording filter: SEG low-frequency workshop, Expanded Abstracts, Session 6.

Dellinger, J. A. and J. Yu, 2009, Low-frequency virtual point-source interferometry using conventional sensors: 71st Meeting, European Associated of Geoscientists and Engineers, Expanded Abstracts, Expanded Abstracts, X047.

Kommedal, J. H., O. I. Barkved, and D. J. Howe, 2004, Initial experience operating a permanent 4C seabed array for reservoir monitoring at Valhall: SEG Technical Program Expanded Abstracts, **23**, 2239–2242.

Landes, M., N. M. Shapiro, S. Singh, and R. Johnston, 2009, Studying shallow seafloor structure based on correlations of continuous seismic records: SEG Technical Program Expanded Abstracts, **28**, 1693–1697.

Lin, F. C., M. H. Ritzwoller, and R. Snieder, 2009, Eikonal tomography: surface wave tomography by phase front tracking across a regional broad-band seismic array: Geophys. J. Int., **177**, 1091–1110.

Longuet-Higgins, M. S., 1950, A theory of the origin of microseisms: Phil. Trans. R. Soc. Lond. A, **243**, 135.

Moreau, J.-P., 2011, Programs concerning matrixes in fortran 90: http://jean-pierre.moreau.pagesperso-orange.fr/. (last visited: January 12, 2011).

NMI, 2011, Norwegian Meteorological Institute climate data database: http://sharki.oslo.dnmi.no/. (last visited: January 12, 2011).

Olofsson, B., 2010, Marine ambient seismic noise in the frequency range 1–10 hz: The

Leading Edge, **29**, 418–435.
Press, W. H., B. P. Flannery, S. A. Teukolsky, and W. T. Vetterling, 1986, Numerical recipes: Cambridge University Press.
Rhie, J. and B. Romanowicz, 2004, Excitation of earth's continuous free oscillations by atmosphere-ocean-seafloor coupling: Nature, **431**, 552–556.
———, 2006, A study of the relation between ocean storms and the earths hum: Geochem. Geophys. Geosyst., **7**, Q10004.
Sandwell, D. T., 1987, Biharmonic spline interpolation of GEOS-3 and SEASAT altimeter data: Geophys. Res. Let., **14**, 139–142.
Sirgue, L., O. I. Barkved, J. Dellinger, J. E. U. Albertin, and J. H. Kommedal, 2010, Full waveform inversion: the next leap forward in imaging at Valhall: First Break, **28**, 65–70.
Tarantola, A., 2006, Elements for Physics - Quantities, Qualities, and Instrinsic Theories: Springer.
Wapenaar, K. and J. Fokkema, 2006, Green's function representations for seismic interferometry: Geophysics, **71**, SI33–SI46.
Wessel, P., 2009, A general-purpose Green's function-based interpolator: Computers & Geosiences, **35**, 1247–1254.

APPENDIX: BICUBIC SPLINE REGUARIZATION

Bicubic spline interpolation is method of interpolation and regularization that relies on fitting the data by a set of weighted Green's functions for cubic cplines (Sandwell, 1987). It is intuitively comparable to bending a metal plate to fit through desired points, by applying and positioning different weights at positions along the plate. The Green's function for a cubic spline with forcing at $\delta(\mathbf{x})$ satisfies

$$\nabla^4 G(\mathbf{x}) = \delta(\mathbf{x}). \tag{12}$$

To fit N datapoints using N forcing functions weighted by w_j, we have the system

$$\nabla^4 d_i(\mathbf{x}) = \sum_{j=1}^{N} w_j \delta(\mathbf{x}_i - \mathbf{x}_j). \tag{13}$$

Using the defined Green's function, we have the system

$$d_i(\mathbf{x}) = \sum_{j=1}^{N} w_j G(\mathbf{x}_i - \mathbf{x}_j), \tag{14}$$

or in matrix notation

$$\mathbf{d} = \mathbf{G}\mathbf{w}, \tag{15}$$

where $G_{ij} = G(\mathbf{x}_i - \mathbf{x}_j)$ is a kernel with Green's functions. The system is solved using an f90 library that performs LU decomposition (Moreau, 2011; Press et al., 1986).

Green's function solutions for cubic splines in various dimensions have been derived and are summarized by Wessel (2009). This paper uses the two dimensional solution

$$G(\mathbf{x}_i - \mathbf{x}_j) = r^2 \left(\ln r - 1 \right), \tag{16}$$

where $r = |\mathbf{x}_i - \mathbf{x}_j|$.